

## REFLECTION MODE DIFFRACTION TOMOGRAPHY

B.A. Roberts and A.C. Kak

Purdue University  
School of Electrical Engineering  
W. Lafayette, IN 47907

A reconstruction algorithm is presented which possesses a simple scanning geometry and promises higher resolution than conventional transmission mode diffraction tomography algorithms. This broad-band reflection mode algorithm inherently lacks a certain amount of low frequency information but an estimate of the information is recovered by spectral extrapolation. The resolution of the algorithm will be shown to be limited by the bandwidth and physical size of the single plane wave transducer, as well as the Born approximation. © 1985 Academic

Press, Inc.

**Key words:** Diffraction tomography; reflection mode; single plane wave transducer; spectral estimation.

### I. INTRODUCTION

Many different approaches to reflection mode tomography have been proposed in the literature. The first of which we would like to mention is the paper presented by Johnson et al. [1] which discusses a ray tracing approach to synthetic aperture reflection imaging. The approach does correct for refraction and attenuation but does not take into consideration diffraction effects and is aimed at tissue parameterization. Secondly, the work of Norton and Linzer [2] analyzes backprojection methods for reconstructing cross-sectional images of ultrasonic reflectivity. The data necessary for reconstruction is obtained from continuous wave scattered field measurements. Also Norton and Linzer [3] presented 3-dimensional inversion equations that were based upon the use of broad-band, pulsed, point sources/receivers. These equations are based upon the Born approximation and are obtained for 3 different scanning geometries. The final form of the equations is that of filtered backprojection. Reconstructions of ultrasonic reflectivity from experimental data have been carried out with good results by K. Dines [4].

A third source of reflection mode imaging work comes from Azimi et al. [5] which considers the reflection mode version of a synthetic aperture reconstruction algorithm proposed in [6]. The approach is based upon the Born approximation and requires only two rotational views of the object. This benefit is offset by the additional complexity of obtaining the scattered field measurements.

Typically, reflection mode tomography suffers from a lack of low frequency information, as will be shown later, but it benefits from the higher frequency content which provides greater spatial resolution. All of the techniques mentioned in the previous paragraph suffer from a lack of low frequency information inherent in reflection mode imaging and/or the lack of consideration of diffraction effects.

In this paper, an algorithm will be presented that reaps the benefits of higher resolution without the sacrifice of low frequency information. This is accomplished with broadband insonification and a spectral extrapolation technique. The spectral extrapolation technique used within this paper is the Gerchberg-Papoulis, GP, algorithm which has been discussed by many authors [7,8,9]. The paper by Sato et al. [10] provides computer simulations of the GP algorithm extended to two dimensions.

The choice of the GP algorithm for use in extrapolating our simulated frequency domain data is based on its simplicity and power. An approach such as the maximum entropy, ME, technique is not suited to the needs of our problem; the ME technique is applicable only to non-negative functions and unfortunately the Fourier domain data we need to extrapolate fails this condition. The ME technique is well suited to the extrapolation of power spectra and digitized images consisting of positive gray levels.

In this paper, spectral extrapolation will be carried out in only one dimension although our problem is inherently two dimensional. Limitation to one dimension is possible because of the symmetry of the object that is used in the computer simulations of the algorithm. Note that when such a symmetry, as will be discussed, is not available, 2-D spectral extrapolation is necessary.

In the subsequent text, the fundamental equations and definitions will first be provided to give the reader a brief background consisting of the Fourier diffraction theorem in reflection mode, the object model used, and the assumptions necessary.

## II. DEFINITIONS AND THEORETICAL PRELIMINARIES

Fundamental to diffraction tomography is the time-independent inhomogeneous wave equation upon which the Fourier diffraction theorem is based and in which  $u(\bullet)$  is the total pressure field and  $k_0$  is the spatial frequency.

$$\nabla^2 u(\vec{r}) + k_0^2 u(\vec{r}) = -k_0^2 f(\vec{r}) u(\vec{r}) \quad (1)$$

The function  $f(\bullet)$  is the scattering potential for which, in the acoustics case, we make the simple choice

$$f(\vec{r}) = \left[ n^2(\vec{r}) - 1 \right],$$

where  $n(\bullet)$  is the complex refractive index at position  $\bar{r}$ . Refractive index will be defined as the ratio  $c_0/c(\bar{r})$ , where  $c_0$  is speed of sound within the medium. This choice of object model prevents us from obtaining distinct reconstructions of compressibility and density upon which speed of sound, and therefore refractive index, depend. For a discussion on the reconstruction of separate density and compressibility images, the reader is referred to [11].

Since it is easier to deal with an integral formulation of the inverse problem, we now make use of the standard Green's function technique along with an unbounded medium assumption to convert Eq. (1) into

$$u_s(\bar{r}) = k_0^2 \int_R u(\bar{r}_0) f(\bar{r}_0) g_k(\bar{r} | \bar{r}_0) d\bar{r}_0 . \quad (2)$$

The free space Green's function is  $g_k(\bullet)$  and the region  $R$  is the finite region of support of the object outside of which  $f(\bullet)$  is equal to zero. Note that the above assumes that the total field is modeled as the superposition of the incident field,  $u_i$ , and the scattered field,  $u_s$ , and that  $u_i$  satisfies a homogeneous wave equation.

$$\nabla^2 u_i(\bar{r}) + k_0^2 u_i(\bar{r}) = 0 .$$

The more general case of a inhomogeneous but known medium is considered in relation to the generalized radon transform, GRT, theory presented by Beylkin [12,13]. For the general case of an inhomogeneous background refractive index  $n_0(\bar{r})$ , the weight function [14] used in the inverse GRT can't be obtained analytically but rather it is determined by ray tracing.

In general, the solution for  $f(\bar{r}_0)$  in Eq. (2) is quite difficult and requires variational methods. However, with the use of the Born approximation, which assumes that the object is weakly scattering,  $|u_s| \ll |u_i|$ , the problem is simplified. This approximation allows us to replace the total field in Eq. (2) by the incident field to yield

$$u_s(\bar{r}) = k_0^2 \int_R u_i(\bar{r}_0) f(\bar{r}_0) g_k(\bar{r} | \bar{r}_0) d\bar{r}_0 . \quad (3)$$

As mentioned in the introduction, the source used in the algorithm to be presented is broadband, but in the remainder of this section we will consider a monochromatic plane wave source. This does not distract from our goal since, in effect, the spectrum of the broadband source,  $U(\bar{r})$  can be modeled as many weighted monochromatic sources,

$$U(\bar{r}) = \int_{k_{z_1}}^{k_{z_2}} A(\alpha) \exp(j\alpha \vec{e}_0 \cdot \bar{r}) d\alpha .$$

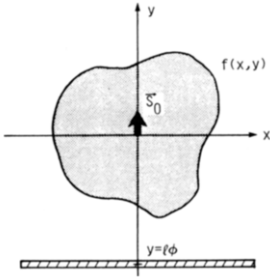


**Fig.1** The scanning geometry used in obtaining backscattered field measurements for use in the SBPWRM algorithm. The single plane wave transducer lies on the line  $y=l_0$ .

The variable  $\bar{s}_0$  is a unit vector in the direction of propagation of the plane wave.

In the remainder of this paper, discussion of the problem will be restricted to two-dimensions in which the free-space Green's function is

$$g_k(\bar{r} | \bar{r}_0) = \frac{j}{4} H_0(k_0 | \bar{r} - \bar{r}_0 | ) ,$$

where  $H_0(\bullet)$  is the zero order Hankel function of the first kind. This Green's function is the solution of the wave equation having a line source at location  $\bar{r}_0 = (x_0, y_0)$  as the forcing function. If use is made of the angular spectrum expansion of  $H_0(\bullet)$ ,  $g_k(\bullet)$  can be rewritten as

$$g_k(\bar{r} | \bar{r}_0) = \frac{j}{4\pi} \int_{-\infty}^{\infty} dK_x \frac{1}{\gamma} e^{j[K_x(x-x_0) + \gamma|y-y_0|]} , \quad \gamma = \sqrt{k_0^2 - K_x^2} . \quad (4)$$

At this point, the above equation has locked us into the geometry illustrated in figure (1), where  $\bar{s}_0$  is pointed in the positive y direction and the receive/transmit transducer is at  $y = l_0$ . This geometry will not prove to be restrictive since a simple rotation of the axes results in object insonification from any desired angle. The goal of this formulation of the problem is to obtain a linear relationship between the scattered field and the scattering potential that can be used to reconstruct the scattering potential.

If both the plane wave expression for  $u_i(\bullet)$  and the angular spectrum expansion of  $g_k(\bullet)$  are inserted into Eq. (3), the result is

$$u_s(x, l_0) = \frac{jk_0^2}{4\pi} \int_{-\infty}^{\infty} dK_x \frac{1}{\gamma} e^{jK_x x} \iint_R f(x_0, y_0) e^{jK_x x_0} e^{j\gamma|y-l_0|} e^{j\gamma y_0} dy_0 dx_0 . \quad (5)$$

As specified in figure (1), the line of receiving transducers is located at  $y = l_0$ , which lies below all  $y \in R$ . This allows us to make the substitution

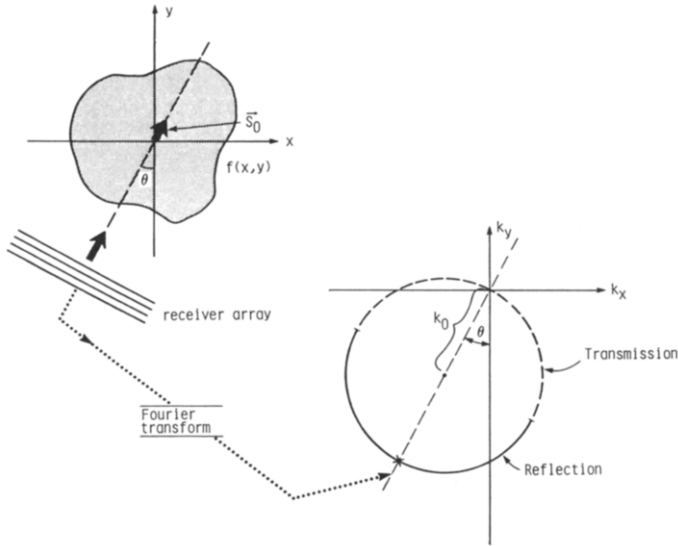


**Fig.2** The Fourier diffraction theorem is illustrated in reflection mode. In transmission mode the forward scattered field is linearly related to the 2D Fourier domain data lying on the dashed line.

$|y_o - l_o| = y_o - l_o$ . The second observation to be made is that for nonevanescant waves,  $k_o > K_x$ , the integrations in Eq. (5) will Fourier transform  $f(\bullet)$ . The result is

$$u_s(x, l_o) = \frac{jk_o^2}{4\pi} \int_{-\infty}^{\infty} dK_x \frac{1}{\gamma} e^{jK_x x} F(K_x, -\gamma - k_o) e^{-j\gamma l_o} , \quad (6)$$

where  $F(\bullet)$  is the Fourier transform of  $f(\bullet)$ . The final step in obtaining the linear relationship that we are searching for, the Fourier diffraction theorem in reflection mode, is to take the spatial Fourier transform of both sides of Eq. (6) with respect to  $x$ :

$$U_s(\beta, y=l_o) = \frac{jk_o^2}{2} \frac{e^{-j\sqrt{k_o^2 - \beta^2} l_o}}{\sqrt{k_o^2 - \beta^2}} F(\beta, -\sqrt{k_o^2 - \beta^2} - k_o) . \quad (7)$$

This final relationship is the crux of reflection mode diffraction tomography as presented in this paper. The significance of this relationship is illustrated in figure (2). The Fourier transform of the backscattered field corresponds to the scaled, phase shifted, spatial Fourier transform of the scattering potential along an arc. The arc is one half of the Ewald circle centered at  $-k_o e_o$ . The data lies on the semicircle because of our choice of  $\beta \leq k_o$  which was necessary to obtain

Eq. (6). Therefore, the arguments of  $F(\cdot, \cdot)$  in Eq. (7) map out a semicircle as  $\beta$  varies from  $-k_0$  to  $k_0$ .

For the sake of completeness, we point out that the Fourier diffraction theorem in transmission mode provides a relationship between the forward scattered field and  $F(u, v)$ . The Fourier transform of the forward scattered field is equal to the scaled, phase shifted, spatial Fourier transform of the scattering potential along the dashed portion of the Ewald circle in figure (2).

### III. SINGLE BROADBAND PLANE WAVE REFLECTION MODE (SBPWRM) RECONSTRUCTION ALGORITHM

#### (a) Mathematical description

For the SBPWRM algorithm presented within this paper, only one phase sensitive plane wave transducer is used. The transducer serves as the source and receiver of broadband acoustical energy and acts to integrate the field impinging upon its surface. Hence, the output of the transducer,  $P_\theta(y=l_0, \omega)$ , can be described as follows,

$$P_\theta(y=l_0, \omega) = \int_{L_m}^{L_m} u_s(x, y=l_0) dx \quad , \quad (8)$$

where  $2L_m$  is the total length of the transducer and  $\theta$  is the angle between the vector  $\mathbf{s}_0$  and the positive  $y$  axis. As  $L_m$  goes to infinity, the transducer output happens to be equal to the zero frequency component of the Fourier transform of the scattered field,  $P_\theta(y=l_0, \omega) = U_s(\beta, y=l_0)$  with  $\beta = 0$ . Therefore, making use of Eq. (8), Eq. (7) can be rewritten with  $\beta = 0$  to yield

$$P_{0^\circ}(y=l_0, \omega) = \frac{jk_0}{2} e^{-jk_0 l_0} F(0, -2k_0) \quad . \quad (9)$$

The above equation provides us with a linear relationship between the scattering potential and the output of the transducer. With the one new assumption that the transducer is long enough to sense nearly all of the backscattered field, Eq. (9) becomes the basis of the reconstruction algorithm.

Given the output of the transducer, the above equation tells us that the single point in the scattering potential's spatial frequency domain, marked by an 'x' in figure (2), is known. Note that the relationship is dependent upon temporal frequency,  $\omega = k_0 c_0$  where  $c_0$  is equal to the speed of propagation in the medium.

If Eq. (9) is implemented at multiple temporal frequencies for a particular rotational position of the transducer,  $\theta$ , what we obtain is an estimate of the scattering potential along a line in the spatial frequency domain. The coverage for fixed  $\theta = 0^\circ$  is illustrated in figure (3) and results from the changing radius of

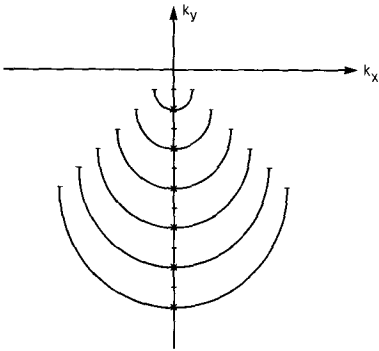


**Fig.3** A monochromatic insonification at six different temporal frequencies would yield the Fourier domain coverage indicated by the semicircles.

the Ewald circle as temporal frequency changes. By rotating the transducer about the object, the line of coverage rotates too, thereby filling in the frequency domain of the scattering potential. Data collection is fast and simple. Figure (4) illustrates the obtainable frequency domain coverage by the area between the two dashed circles centered at the origin. Obviously, low frequency content is missing.

(b) Computer simulation (without spectral estimation)

To simulate the algorithm, it is necessary to use an object for which an exact expression for the scattered field is obtainable. For this reason, the object used is a constant refractive index cylinder for which the scattered field is exactly known, [15].

Generating the data necessary to fill the frequency domain consists of calculating the scattered field for each temporal frequency within the bandwidth of the transducer. This calculation needs to be done only for one angular

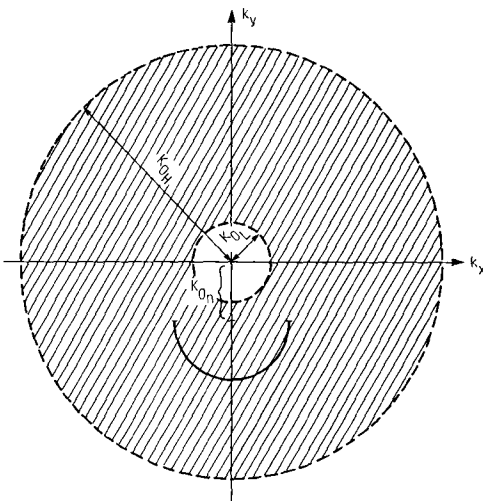


**Fig.4** The slice of the scattering potential's frequency spectrum that is theoretically obtainable with the SBPWRM algorithm. Note that  $\lambda$ , as used in this paper, will be defined as  $\frac{2\pi}{k_{OH}}$ .

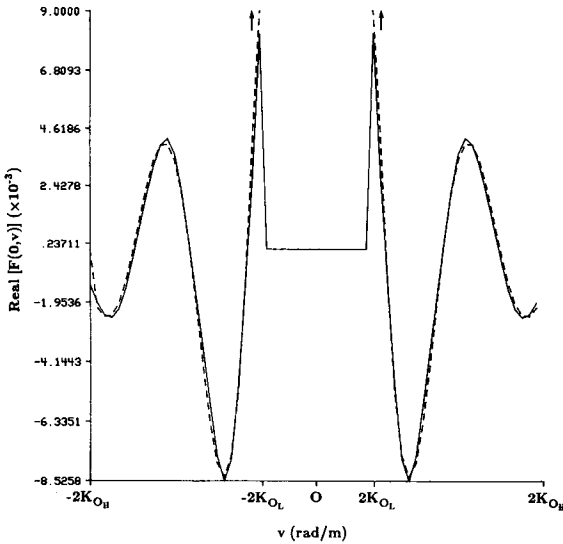


**Fig.5** A comparison of the true slice of the scattering potential's frequency spectrum (dashed line) and the slice obtained from the SBPWRM algorithm. The object in this figure is a cylinder of constant refractive index 1.01 and a radius of  $1\lambda$  ( $\lambda$  is defined in the previous figure caption and in the text).

position of the transducer since the object is circularly symmetric as is the spatial frequency domain of the scattering potential. Figure (5) is a plot of the real part of the slice of the frequency domain coverage obtained from a single measurement of the broad-band scattered field from a cylinder. In this case, the cylinder is of radius  $1\lambda$  and has a refractive index of 1.01. Note that the center of the plot is where the zero frequency component is located and that  $2k_{OH}$  is the highest spatial frequency obtainable. The value of  $\lambda$  that is referred to above is by our definition  $2\pi/k_{OH}$ . The solid line in the plot is the result obtained with simulated scattered field data and the dashed line is the true slice of the real part of the scattering potential's Fourier transform. The coverage provided seems quite good within the range of spatial frequencies for which data can be obtained. Note that the solid line simulates the data that could be obtained from a transducer that has a bandwidth of approximately 1.2 MHz and a center frequency of 1 MHz. This particular transducer bandwidth will be used in all subsequent simulations.

Likewise, figure (6) presents a plot of a slice of the real part of the frequency spectrum obtained when the object is a  $1\lambda$  cylinder with a refractive index of 1.1. The reader will most likely notice that the data obtain for the cylinder of higher refractive index does not match the exact frequency domain coverage. This fault is due solely to the 1st Born approximation.

When many such broad-band scattered field measurements, where each measurement results in a slice of  $F(u,v)$ , are obtained by rotating the transducer about the object, enough data is obtained to essentially reconstitute  $F(u,v)$ . This is quite similar to imaging with non-diffracting sources of insonifying energy for which the popular reconstruction approach is filtered backprojection [16]. In this paper, consideration is given only to direct filling of the frequency space with the aid of bilinear interpolation followed by two-dimensional Fourier inversion.

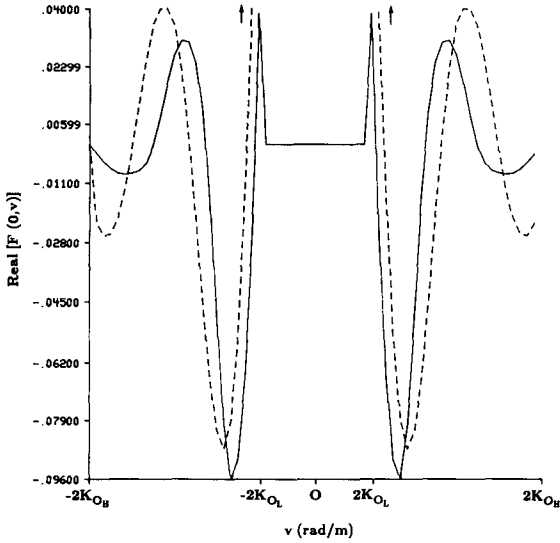


**Fig.6** A comparison of the true slice of the scattering potential's frequency spectrum (dashed line) and the slice obtained from the SBPWRM algorithm. The object in this figure is a cylinder of constant refractive index 1.1 and a radius of  $1\lambda$ .

The plots in figures (7) and (8) are the real parts of the reconstructions of two cylinders both having a radius of  $1\lambda$  but having refractive indices of 1.01 and 1.1 respectively. For clarity, the center slice of each reconstruction is provided in part (b) of each figure. In figure (7)(b), the dashed line indicates the true center slice of the scattering potential. Figure (8)(b) does not contain the true center

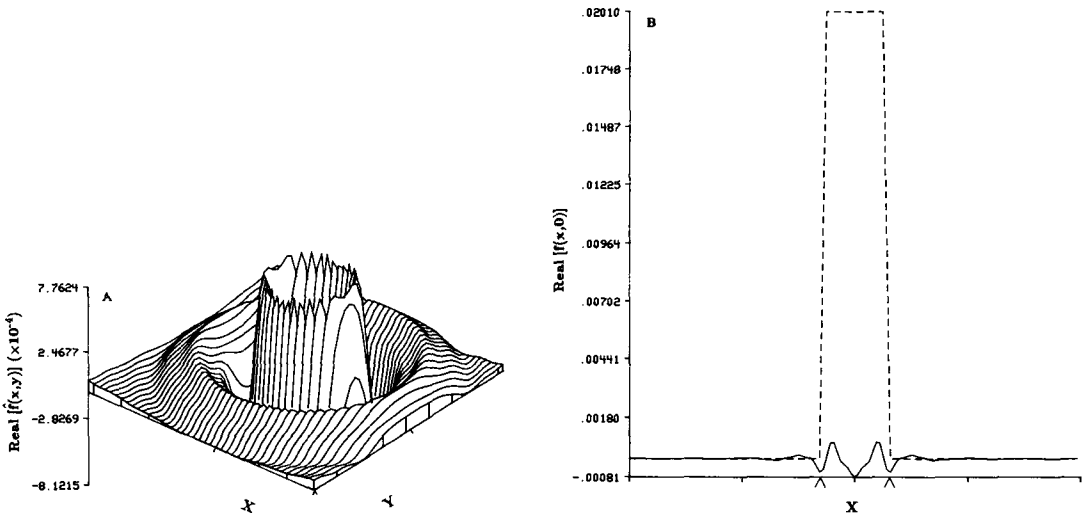


**Fig.7** The real part of the reconstruction of a cylinder of radius  $1\lambda$  having a 1.01 refractive index. This reconstruction does not make use of any kind of spectral estimation. Only the frequency domain coverage obtained from the backscattered field is utilized. Part (a) is a 2-dimensional plot and (b) is center slice of the reconstruction. The dashed line is the true slice and the edges of the object are marked by  $\hat{\phantom{x}}$  symbols.

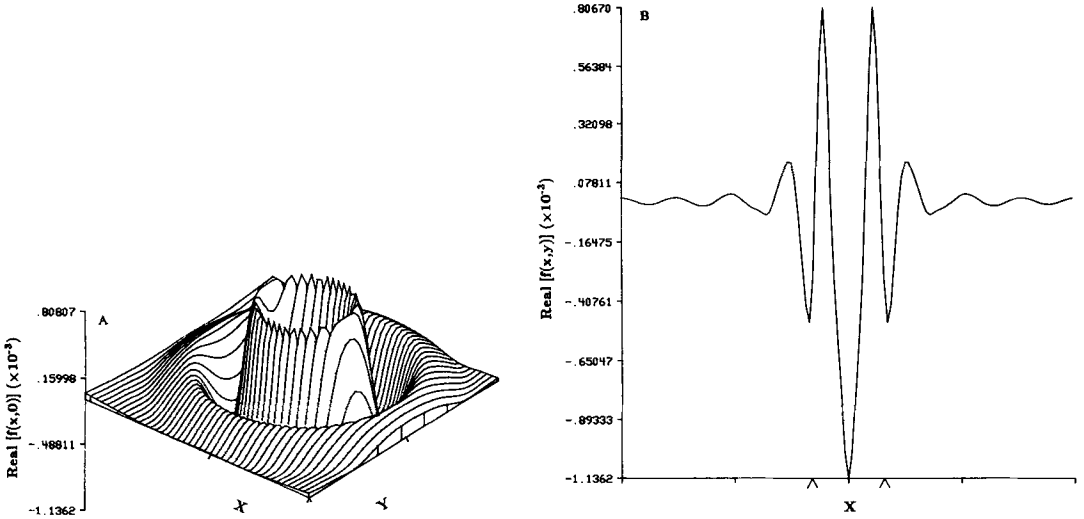


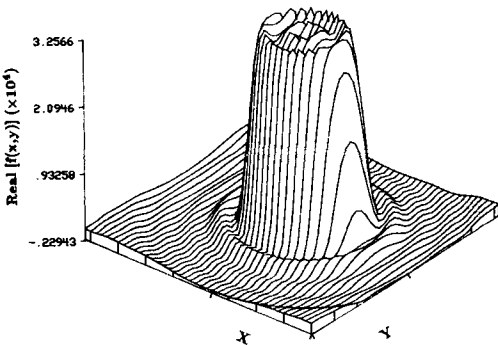
Fig.8 The real part of the reconstruction of a cylinder of radius  $1\lambda$  having a 1.1 refractive index, (a) 2-dimensional plot, (b) center slice of the reconstruction. The edges of the object are marked by ^ symbols.

slice due to the fact that the reconstructed slice has a magnitude that is prohibitively small. Note that in the center slice plots, the ^ symbols point out the locations of the boundary of the cylinder. The only observable merit of the reconstructions lies in their specification of the discontinuities in refractive index which occur at the object boundary.

It is interesting to note that the lower frequencies that are missing in the reconstructions cause the reconstructions to somewhat resemble the first derivative of the scattering potential.

For pedagogical purposes, figure (9) is theoretically the best reconstruction obtainable with the algorithm. Note that we have used the whole temporal

Fig.9 The real part of the reconstruction of a cylinder of radius  $1\lambda$  having a refractive index of 1.01. An "infinite" bandwidth transducer has provided the frequency domain data for this reconstruction. Note that bilinear interpolation has been used to approximate the zero frequency sample of the frequency domain before Fourier inversion.



frequency range to insonify the object. From the extremely wide bandwidth scattered fields, all the samples of  $F(u,v)$  are obtained except for the zero frequency component which is estimated by simple interpolation. Unfortunately, the amplitude of this real portion of the reconstruction is far from accurate (0.0201) due to the poor filling of the frequency domain near zero frequency.

The next section of this presentation considers the use of spectral estimation techniques to gain some knowledge about the missing part of the spectrum  $F(u,v)$ .

#### IV. SPECTRAL ESTIMATION

What follows is a short summary of a few of the best known approaches to spectral estimation that seem to be favored in the literature. This will in no way be an exhaustive nor a detailed survey of spectral estimation. The only goal is to give the reader some background and describe the approach used within this paper. Very thorough and precise references have been provided for the interested reader in the introduction and in the following text.

The basic concept that enables the Gerchberg-Papoulis technique of spectral extrapolation to function is the analytic property of the spectrum being extrapolated. In reference [17], the following theorems are stated and proven:

- 1.) A function that is analytic in a domain  $D$  is uniquely determined over  $D$  by its values over a domain, or along an arc, interior to  $D$ .
- 2.) If two analytic functions,  $f_1$  and  $f_2$ , with the domains  $D_1$  and  $D_2$ , have a region of intersection,  $D_1 \cap D_2$ ,  $f_1$  must equal  $f_2$  in the region of intersection. It follows from the first theorem that the two functions are identical over both  $D_1$  and  $D_2$ .

##### (a) Gerchberg-Papoulis (GP) algorithm

This iterative algorithm combines the analytic nature of the spectrum, *a priori* spatial information and a known range of the spectrum obtained from scattered field measurements, to iteratively obtain the full spectrum. In our application, the known region of the Fourier domain,  $H(u,v)$ , obtained from the scattered field, is a bandpass function which sets our application apart from the typical low-pass frequency range that is considered in the literature. The knowledge of  $H(u,v)$  and the finite region of support of the object, is all that is necessary to begin iterating. The first estimate of  $f(x,y)$  is generated by the inverse transformation of  $H(u,v)$  which yields  $h_0(x,y)$ . The following steps outline the GP algorithm:

- i.) The first step of the iteration consists of multiplying  $h_{n-1}(x,y)$  by the region of support function,  $P(x,y)$

$$P(x,y) = \begin{cases} 1 & \text{if } (x,y) \in R \\ 0 & \text{if otherwise} \end{cases}$$

to yield the function  $f_n(x,y)$ .

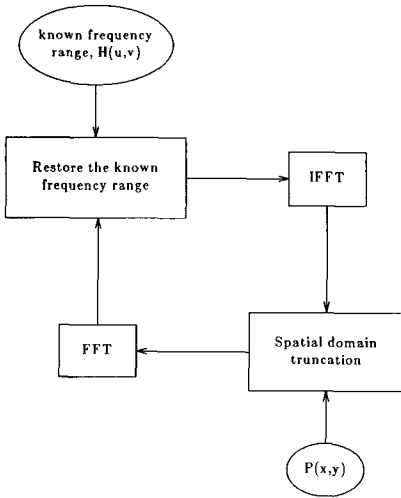


Fig.10 A block diagram of the steps taken in the Gerchberg-Papoulis algorithm of spectral extrapolation.

- ii.) Secondly,  $f_n(x,y)$  is transformed resulting in  $F_n(u,v)$ .
- iii.) Thirdly, the region in which  $F(u,v)$  is known is restored to its original value,  $H(u,v)$ , without disturbing the remainder of the frequency domain. The result of this step we shall call  $H_n(u,v)$ .
- iv.) Finally,  $H_n(u,v)$  is inverse transformed to obtain  $h_n(x,y)$  and we return to step (i) to generate the  $(n+1)$ th estimate.

To aid in the description, a block diagram of the algorithm is provided in figure (10). Also for the sake of clarity, the relationships in the above steps are outlined below.

$$H_n(u,v) = \begin{cases} H(u,v) & , (u,v) \in L \\ F_n(u,v) & , \text{otherwise} \end{cases}$$

$$F_n(u,v) = \int_{-\infty}^{\infty} \int_{-\infty}^{\infty} f_n(x,y) e^{-j(ux+vy)} dx dy$$

$$= \int_R h_{n-1}(x,y) e^{-j(ux+vy)} dx dy .$$

In the above,  $L$  is the region in which  $H(u,v)$  is nonzero and  $R$  is the spatial domain region of support of the object.

Following the presentation in [7], the mean square error of the estimate  $f_n$ , within one iteration, is twice reduced. With the aid of Parseval's equation, the following relationships hold:

$$\int_{-\infty}^{\infty} \int_{-\infty}^{\infty} |f(x,y) - h_{n-1}(x,y)|^2 dx dy > \int_{-\infty}^{\infty} \int_{-\infty}^{\infty} |f(x,y) - f_n(x,y)|^2 dx dy =$$

$$= \int_{-\infty}^{\infty} \int_{-\infty}^{\infty} |F(u,v) - F_n(u,v)|^2 du dv > \int_{-\infty}^{\infty} \int_{-\infty}^{\infty} |F(u,v) - H_n(u,v)|^2 du dv .$$

The inequalities are, of course, due to the relationships  $|f(x,y)-h_{n-1}(x,y)| > |f(x,y)-f_n(x,y)|$  and  $|F(u,v)-F_n(u,v)| > |F(u,v)-H_n(u,v)|$  that result from spatial limiting and frequency range restoration, respectively.

One possible iteration stopping criteria for the algorithm is

$$E_n = \int_{-\infty}^{\infty} \int_{-\infty}^{\infty} |f_n(x,y)-f_{n-1}(x,y)|^2 du dv < \delta , \quad (10)$$

where  $\delta$  is an acceptably small mean square error between iterations.

As shown in [9], the spectrum extrapolated by the GP algorithm has a resolution that is severely limited by the accuracy of the known frequency range but doesn't seem to be sensitive to noise.

In the paper by Sezan and Stark [18], the GP algorithm is reformulated such that extrapolation is accomplished by iteratively projecting onto convex sets. This approach enables each constraint involved in the algorithm to be incorporated as a projection onto a set of functions satisfying that particular constraint. The beauty of this approach is in its ability to easily include many constraints on the extrapolation. Additional information on the method of projection onto convex sets is provided in [19,20].

#### (b) Series Expansion and Analytic Continuation

A second approach, as presented in [21], depends upon the spatially limited nature of the object which also implies that the object has an analytic spectrum. This approach uses the sampling theorem in the frequency domain and requires only discrete samples within the known range of the frequency domain.

If a two-dimensional object,  $f(x,y)$ , is spatially limited such that  $-A < x < A$  and  $-B < y < B$ , the spectrum  $F(u,v)$  can be represented as follows:

$$F(u,v) = \sum_{m=-\infty}^{\infty} \sum_{n=-\infty}^{\infty} F_{mn} \operatorname{sinc}\left(\frac{m}{A} - u\right) \operatorname{sinc}\left(\frac{n}{B} - v\right) .$$

Harris [21] has demonstrated that a useful approximation to  $F(u,v)$  is obtained even when the series is severely truncated. In other words, the spectrum is being represented by a finite number of its Fourier coefficients.

The approach suffers greatly when the known frequency content is noisy and the situation is complicated further when only a small range of the frequency domain, from which values of  $F_{mn}$  are obtained, is known.

#### (c) Linear Prediction Estimator

The least mean square error linear prediction method, as presented by Gabriel [22], uses a  $K$  point prediction filter to estimate samples of the one

dimensional functions  $F(u)$  and  $|F(u)|^2$ . This approach has been shown to be equivalent to Burg's maximum entropy method [23] of power spectrum estimation in the paper by Van den Bos [24]. However, in our application, we are not interested in the power spectrum  $|F(u)|^2$  but instead we wish to estimate  $F(u)$  which is typically complex. In the following, it is assumed that the function  $F(u)$  is real.

The K point prediction filter takes the form

$$\hat{F}_n = \sum_{m=1}^K A_m F_{n-m} , \quad (11)$$

in which  $\hat{F}_n$  is the estimate of the nth sample of  $F_n$ . To design the prediction filter the error involved in this estimate, expressed by

$$\epsilon_n = F_n - \hat{F}_n ,$$

is minimized in the mean square sense. Taking the sum of the error terms yields

$$E = \sum_{i=1}^K \epsilon_n ,$$

which must be minimized with the K conditions

$$\frac{\partial E}{\partial A_i} = 0, \quad i = 1, 2, \dots, K .$$

These conditions generate K equations with which to solve for the K unknown filter coefficients. Methods of solving for the K unknowns are presented in [25].

The resulting K coefficients provide us with a filter that causes the power spectrum of  $\epsilon_n$  to be "white." It is in this respect that the linear prediction method resembles the maximum entropy method. The filter's action of "whitening"  $\epsilon_n$ 's spectrum can also be viewed as maximizing the entropy of  $\epsilon_n$ . Hence, as we have very briefly alluded, the maximum entropy method of estimation is closely related to linear predictive estimation. The use of the filter allows us to predict many "smoothed" samples of the spectrum with marginal error given the K previous samples of the spectrum.

The unique facet of the filter is the manner in which it relates to the power spectrum of the function for which it is designed. Notice that the Z transform of Eq. (11) is

$$\hat{F}(Z) = \left[ \sum_{m=1}^K A_m Z^{-m} \right] F(Z) .$$

Hence, the Z transform of the prediction error can be described as

$$E(Z) = \left[ 1 - \sum_{m=1}^K A_m Z^{-m} \right] F(Z) = H(Z) F(Z) .$$

Using the fact that the power spectrum of a white noise function is equal to a constant,  $|\Delta(Z)|^2 = C$ , leads us to the conclusion that the power spectrum of the filter H(Z) is the reciprocal of the power spectrum of F(Z):

$$|F(Z)|^2 = \frac{C}{\left| 1 - \sum_{m=1}^K A_m Z^{-m} \right|^2} .$$

The only foreseeable application of ME to our needs would be the extrapolation of the magnitude of the Fourier transform F(u,v).

## V. THE SBPWRM ALGORITHM WITH SPECTRAL ESTIMATION

In this section, the GP algorithm is used to aid in obtaining the low frequency information unobtainable from the scattered field measurements made for the SBPWRM algorithm described above. The choice of the Gerchberg algorithm is predicated on its efficient implementation which in turn is based upon the fast Fourier transform (FFT). As of the time of publication, no other methods of spectral estimation have been implemented. Note that a study of the range of objects that can be accurately reconstructed has not been done here. For the interested reader a detailed study has been provided by Slaney et al. [26] for the case of transmission mode tomography. Since both reflection and transmission modes suffer from the same assumptions and approximations, there is reason to believe that similar bounds on reconstructable objects can be assumed.

The FFT implementation of the GP algorithm does present the difficulty of having to deal with a simultaneously spatially-limited and band-limited function. Of course, the idea of having a spatially-limited object implies that the spectrum must be infinite in extent. By limiting the function's spectrum, the analytic nature of the spectrum is lost, but with the assumption that the function's spectrum is negligible outside the band-limited region, the analyticity of the spectrum is retained.

The one dimensional slices of the scattering potential's two dimensional Fourier transform obtained from the SBPWRM algorithm's broad band measurements, have been processed by the GP technique with surprising results. Note that the region of support function, P(x), that was used, is equal to 1 for  $|x| \leq 1\lambda$  and 0 elsewhere. Figures (11) and (12) present the extrapolated slices of the real part of the frequency domain obtained for both of the cylinders that

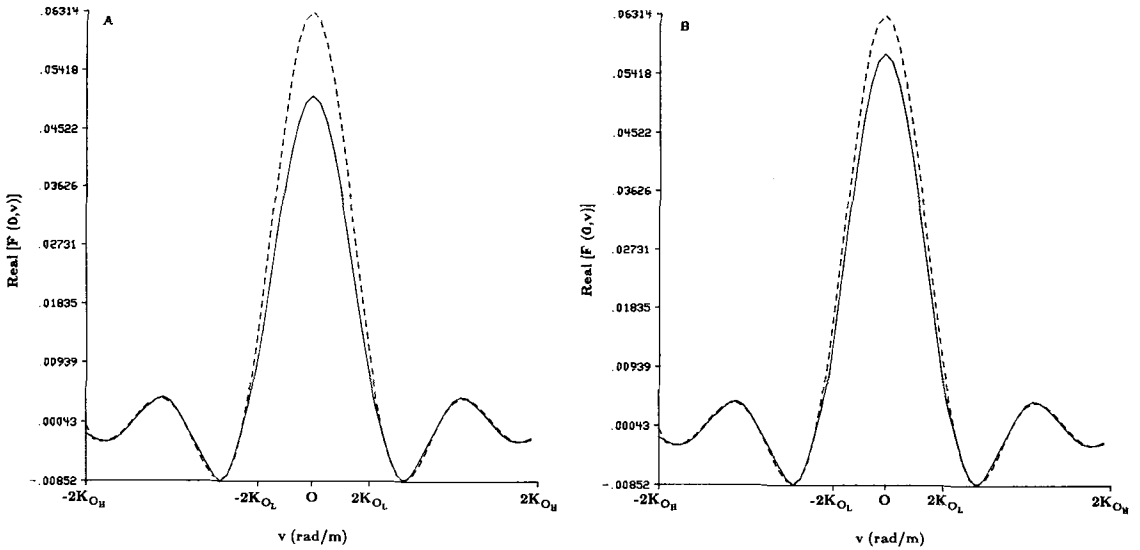


**Fig.11** The result of the GP algorithm applied to the frequency domain slices in figure 5: (a) 150 iterations of the GP algorithm, (b) 250 iterations of the GP algorithm.

were reconstructed previously. Figure (11)(a) is the slice of the cylinder of 1.01 refractive index after 150 iterations and (11)(b) is the result after 250 iterations of the GP algorithm. Likewise, figure (12) presents slices of the cylinder having a

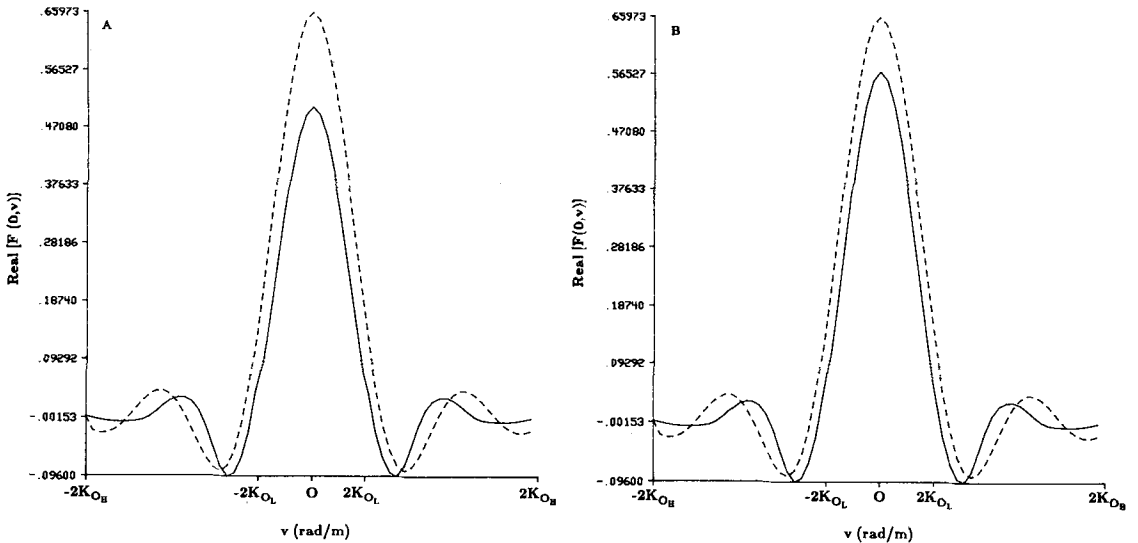


**Fig.12** The result of the GP algorithm applied to the frequency domain slices in figure 6: (a) 150 iterations of the GP algorithm, (b) 250 iterations of the GP algorithm.

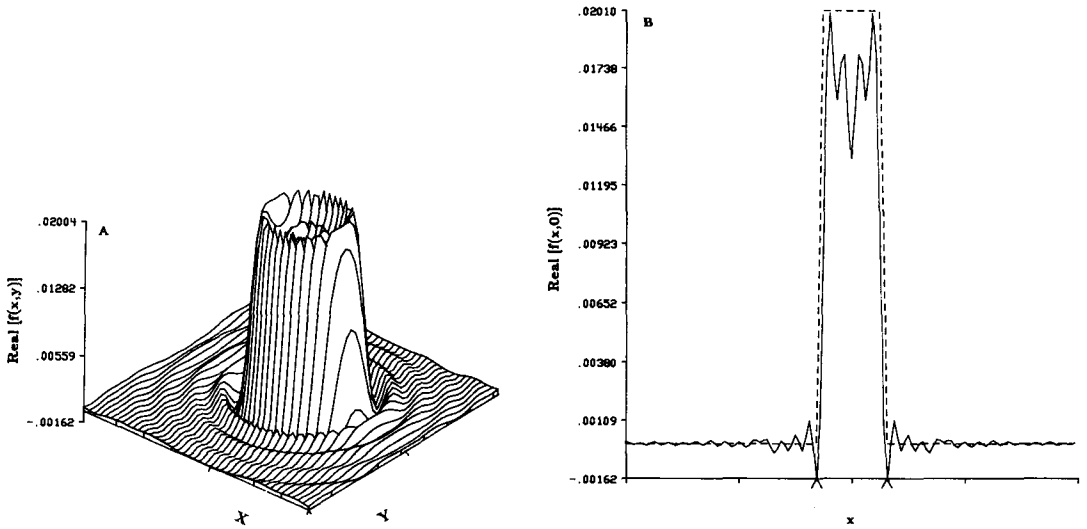


**Fig.13** The real part of the reconstruction obtained with the use of GP enhanced frequency slice in figure 11. Part (b) of the figure is the center slice of the reconstruction compare to the exact slice (dashed line).

1.1 refractive index. It is interesting to note how well the previously unknown frequency range,  $-2k_{oL} < v < 2k_{oL}$  has been estimated.

The number of iterations of GP that are required is quite high but remember that very little information within the object's region of support was provided by the initial frequency domain coverage. Hence, more iterations were required.

In figure (6), it is obvious that the simulated slice deviates from the exact slice and yet extrapolation still provides a very reasonable approximation to the exact slice as shown in figure (12). At first glance the use of the GP technique seems miraculous but beware that the technique will not help at all if it is initially provided with inaccurate data. In other words, the fundamental limiting factor to the accuracy of the approach to diffraction tomography presented in this paper is the Born approximation. If the Born approximation does not hold, the inaccurately known frequency range will be extrapolated by the GP technique into something that remains inaccurate.

The newly extrapolated slices in figures (11) and (12), when used to fill up the two dimensional frequency domain, yield the reconstructions whose real parts are presented in figures (13) and (14). The center slices of each reconstruction appear as solid lines and their exact counterparts as dashed lines in part (b) of each figure. The center slice plots aid in providing an idea of the accuracy of the amplitudes of the reconstructions. Note that these reconstructions are much better than the reconstruction provided by the theoretical limit to the SBPWRM

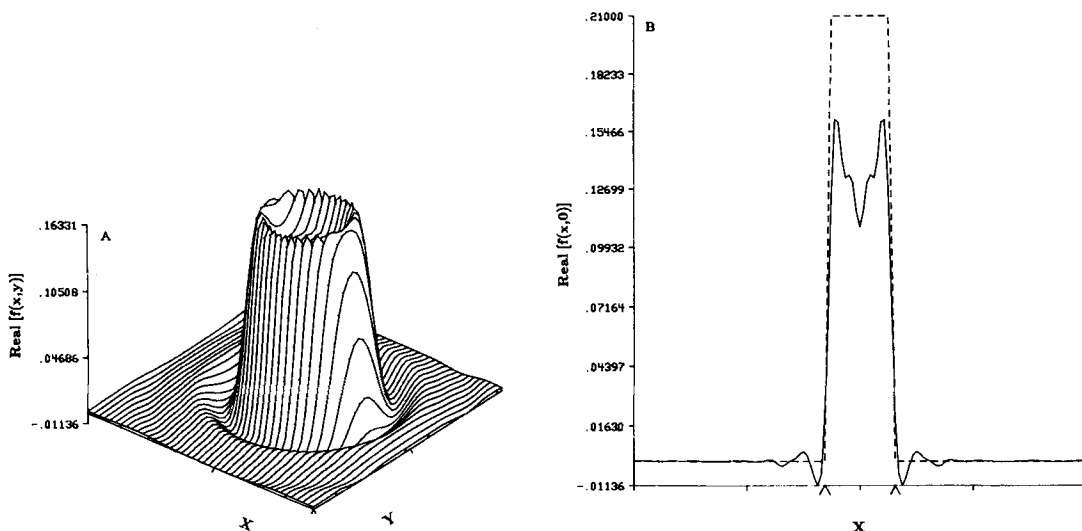


**Fig.14** The real part of the reconstruction obtained with the use of GP enhanced frequency slice in figure 12. Part (b) of the figure is the center slice of the reconstruction compare to the exact slice (dashed line).

algorithm that is presented in figure (9). This is of course due to the more accurate estimation of the frequency domain very near zero frequency.

## VI. CONCLUSION

What has been presented in this paper is a description of a reflection mode diffraction tomography algorithm that makes use of a very simple scanning geometry consisting of a single plane wave transducer. Unfortunately, the algorithm alone suffers from a lack of low frequency information that can only be obtained with the use of spectral extrapolation or with the use of forward scattered field measurements. Hence, we have also explored spectral estimation techniques and have applied the Gerchberg-Papoulis technique to the frequency domain coverage obtained with our algorithm. The results of this application are quite good but the SBPWRM algorithm itself is limited to a range of objects for which the Born approximation holds. Another limitation to the type of objects that can be imaged is the physical size of the plane wave transducer. The transducer must provide a ripple free plane wave to the slice of the object being imaged and it must be long enough such that all of the backscattered field will impinge upon the surface of the transducer.

As briefly mentioned above, the combination of broadband backscattered and forward scattered fields could be used to obtain a nearly complete filling of the scattering potential's frequency domain.

The assumptions used in developing the algorithm are 1) that only backscattering is observed and 2) that only small refractive index objects can be imaged so that Born approximation will hold.

Future work with the SBPWRM algorithm will consist of implementing additional spectral estimation techniques and investigating the use of forward scattered fields in the algorithm. In addition, a study should be done of the range of objects for which the 1st order Born approximation is valid within the algorithm. A study of the limits of 1st order Born and Rytov reconstructions in transmission mode is provided in [26].

#### ACKNOWLEDGEMENT

Many thanks go to M.G. Slaney, Schlumberger Palo Alto Research, for his kind encouragement, support and advice. Likewise, we must thank S.J. Norton, National Bureau of Standards, for his encouragement and advice. This work was supported by grant NIH #HL3192404.

#### REFERENCES

- [1] Johnson, S., Greenleaf, J., Tanaka, M., Rajogopalan, B., and Bahn, R., Quantitative Synthetic Aperture Reflection Imaging with Correction for Refraction and Attenuation: Application of Seismic Techniques in Medicine, in 1978 IEEE Biomedical Symposium Proceedings.
- [2] Norton, S., and Linzer, M., Ultrasonic reflectivity tomography: reconstruction with circular transducer arrays, Ultrasonic Imaging 1 , 154-184 (1979).
- [3] Norton, S., and Linzer, M., Ultrasonic reflectivity imaging in three dimensions: exact inverse scattering solutions for plane, cylindrical and spherical apertures, IEEE Trans. Biomedical Engr. BME-28 , 202-220 (1981).
- [4] Dines, K., Imaging of ultrasonic reflectivity, unpublished work.
- [5] Azimi, M., and Kak, A.C., Multiple Scattering and Attenuation Phenomena in Diffraction Imaging, Technical Report, TR-EE-85-4 , (Purdue Univ., School of Elec. Engr., 1985).
- [6] Nahamoo, D., and Kak, A.C., Ultrasonic Diffraction Imaging, Technical Report, TR-EE-82-20 , (Purdue Univ., School of Elec. Engr., 1982).
- [7] Papoulis, A., A new algorithm in spectral analysis and band-limited extrapolation, IEEE Trans. Circs. Sys. CAS-22 , 735-742 (1975).
- [8] Trussell, H., The feasible solution in signal restoration, IEEE Trans. Acoust. Speech Sig. Proc. ASSP-32 , 201-212 (1984).
- [9] Gerchberg, G., Super-resolution through error energy reduction, Optica Acta 21, 709-720 (1974).

- [10] Sato, T., Norton, S., Linzer, M., Ikeda, O., and Hirama, M., Tomographic image reconstruction from limited projections using iterative revisions in image and transform spaces, Applied Optics **20** , 395-399 (1981).
- [11] Norton, S., Generation of separate density and compressibility images in tissue, Ultrasonic Imaging **5** , 240-252 (1983).
- [12] Beylkin, G., Imaging of discontinuities in the inverse scattering problem by inversion of a causal generalized radon transform, Math. Phys. **26** , 99-108 (1985).
- [13] Beylkin, G., Reconstructing discontinuities in multidimensional inverse scattering problems: smooth errors versus small errors, Applied Optics **24** , 4086-4088 (1985).
- [14] Miller, K., Oristaglio, M., and Beylkin, G., A New Formalism and an Old Heuristic for Seismic Migration, Extended Abstract, 54th Annual International Meeting Society Exploration Geophysics , pp. 704-707, (1984).
- [15] Morse, P.M., and Ingard, K.U., Theoretical Acoustics , p. 464, (McGraw Hill, New York, 1968).
- [16] Kak, A.C., and Roberts, B.A., Reconstructions from Projections: Applications in Computerized Tomography, in Handbook of Pattern Recognition and Image Processing , T.Y. Young and K.S. Fu, eds., , pp. 649-692, (Academic Press, New York, 1986).
- [17] Churchill, R.V., Brown, J.W., and Verhey, R.F., Complex Variables and Applications , pp. 286-289, (McGraw Hill, New York, 1976).
- [18] Sezan, M.I., and Stark, H., Image restoration by the method of convex projections: part 2 - applications and numerical results, IEEE Trans. Med. Imaging **MI-1** , 95-101 (1982).
- [19] Youla, D.C., Webb, H., Image restoration by the method of convex projections: part 1 - theory, IEEE Trans. Med. Imaging **MI-1** , 81-94 (1982).
- [20] Schafer, R.W., Mersereau, R.M., and Richards, M.A., Constrained iterative restoration algorithms, Proc. IEEE **69** , 432-450 (1981).
- [21] Harris, J.L., Diffraction and resolving power, J. Opt. Soc. Amer. **54** , 931-936 (1964).
- [22] Gabriel, W.F., Spectral analysis and adaptive array superresolution techniques, Proc. IEEE **68** , 654-666 (1980).

- [23] Burg, J.P., Maximum Entropy Spectral Analysis, Proc. 37th Meeting Society Exploration Geophysicists , (1967).
- [24] Van den Bos, A., Alternative interpretation of maximum entropy spectral analysis, IEEE Trans. Inform. Theory IT-17 , 493-494 (1971).
- [25] Childers, D.G., ed., Modern Spectrum Analysis , (IEEE Press, New York, 1978).
- [26] Slaney, M.G., Kak, A.C., and Larsen, L.E., Limitations of imaging with first-order diffraction tomography, IEEE Trans. Microwave Thry. Techniques MTT-32 , 1262-1275 (1984).